Optimal Experiment Design for Timelapse Traveltime Tomography

Jonathan B. Ajo-Franklin[*†]

[*]*Earth Science Division,*

Lawrence Berkeley National Laboratory,

1 Cyclotron Rd, Mail Stop 90R116,

Berkeley, CA, 94720

[†]*Formerly Earth Resources Laboratory,*

Dept. of Earth, Atmospheric, and Planetary Sciences,

Massachusetts Institute of Technology,

42 Carleton St, Cambridge, MA 02142

(April 1, 2009)

Running head: **Optimal Timelapse Tomography**

ABSTRACT

Geophysical monitoring techniques offer the only noninvasive approach capable of assessing both the spatial and temporal dynamics of subsurface fluid processes. Increasingly, permanent sensor arrays in boreholes and on the ocean floor are being deployed to improve the repeatability and increase the temporal sampling of monitoring surveys. Because permanent arrays require a large up-front capital investment and are difficult (or impossible) to re-configure once installed, a premium is placed on selecting a geometry capable of imaging the desired target at minimum cost. We present a simple approach to optimizing downhole sensor configurations for monitoring experiments making

use of differential seismic traveltimes. In our case, we use a design quality metric based on the accuracy of tomographic reconstructions for a suite of imaging targets. By not requiring an explicit singular value decomposition of the forward operator, evaluation of this objective function scales to problems with a large number of unknowns. We also restrict the design problem by recasting the array geometry into a low dimensional form more suitable for optimization at a reasonable computational cost. We test two search algorithms on the design problem: the Nelder-Mead downhill simplex method and the Multilevel Coordinate Search algorithm. The algorithm is tested for four crosswell acquisition scenarios relevant to continuous seismic monitoring, a two parameter array optimization, several scenarios involving four parameter length/offset optimizations, and a comparison of optimal multi-source designs. In the last case, we also examine trade-offs between source sparsity and the quality of tomographic reconstructions. One general observation is that asymmetric array lengths improve localized image quality in crosswell experiments with a small number of sources and a large number of receivers. Preliminary results also suggest that high-quality differential images can be generated using only a small number of optimally positioned sources.

INTRODUCTION

Understanding the combined spatial and temporal characteristics of dynamic subsurface processes is a challenge common to many contemporary problems in the geosciences. Examples include the growth of bacterial communities during enhanced remediation, the dissolution of methane hydrates during stimulated production, and the movement of CO_2 during sequestration activities. These are but three of numerous applications which require knowledge of spatio-temporal variability to improve our fundamental understanding of relevant physical processes.

Geophysical monitoring techniques offer the only approach capable of assessing the dynamics of these systems beyond the limited possibilities afforded by direct *in situ* observations. Historically, monitoring datasets have consisted of surveys sequentially collected using acquisition geometries and sensor platforms similar to static measurements e.g. repeated reflection seismic surveys. Unfortunately, a host of logistical constraints hamper the repeatability of such surveys, such as difficulties in exactly replicating the source/receiver geometry, changes in overburden conditions (Vesnaver et al., 2003), and sufficiently matching the seismic processing flow (Ross and Altan, 1997).

Increasingly, permanent sensor arrays in boreholes (Blanco et al., 2006; Daley et al., 2007b) and on the ocean floor (Smit et al., 2006; Thompson et al., 2006) are being deployed to improve the repeatability of monitoring surveys by eliminating the need to re-position receivers. By allowing continuous monitoring, permanently deployed sensor arrays also have the potential to improve the *temporal* resolution of geophysical measurements by an order of magnitude (or more); this increase in temporal sampling will in turn allow scientists to probe transient subsurface processes with shorter time scales, invisible to the currently available 4D seismic monitoring methods that typically sample on the scale of months or even years.

Despite clear data quality advantages, permanent arrays require both substantial up-front capital investments and long-term maintenance and thus necessitate careful analysis to justify their installation. Since permanent arrays are often difficult (or impossible) to re-configure once in-place, their design assumes an even more important role than in the case of more traditional surveys where mistakes can be potentially be corrected during later deployments. For permanent arrays to be a cost-effective monitoring option, emphasis must be placed on selecting the sparsest (and hence least expensive) possible source/receiver geometry capable of producing images of a given quality. Smit et al. (2006) cogently presents this philosophy within the context of ocean bottom cable installations. While the cost of a given geometry is relatively simple to evaluate, the "quality" of the resulting experiment is more difficult to quantify since it depends not only on our ability to resolve individual geologic features but also on the monitoring questions we are attempting to answer. Binary detection of change within a broad region should be an easier task than reconstructing an accurate subsurface image. Designing a good survey is most difficult in cases for which we lack experience e.g. irregular geometries, unusual spatial constraints, or a strongly heterogeneous background, all of which can render typical "rules of thumb" invalid.

Given the central importance of survey geometry in the context of monitoring, we will consider algorithms for the selection of an optimal (or at least improved) configuration from within the space of possible designs. This task falls within the class of problems often referred to as *optimal experiment design*, a field which has proponents in both geophysics (Maurer and Boerner, 1998; Curtis, 1999a,b; Stummer et al., 2002; van den Berg et al., 2003; Curtis et al., 2004; Routh et al., 2005) and the broader scientific community (Box and Lucas, 1959; John and Draper, 1975; Walter and Pronzato, 1987; Muzic et al., 1996). When searching for an optimal experiment several considerations rapidly become apparent, mainly what "optimal" means in the context of geophysical

measurements. Other crucial issues include the range of experimental designs to be considered, the technique used to solve the optimization problem, and the fashion in which design constraints are implemented.

In our approach, we use the l_2 difference between a suite of reference images and the corresponding tomographic reconstructions as a quality measure for a given geometry. This suite of reference images can be selected to mimic either traditional resolution metrics (e.g. checkerboards in our case) or directly linked to the spatial characteristics of the process being monitored. We also adopt a reduced parameterization for describing experimental geometry; instead of allowing sources and receivers to occupy arbitrary locations, we search for an optimal set of secondary descriptive parameters such as array width, orientation, or center location. This approach, while lacking the flexibility of the most general descriptions of experiment geometry, results in a more manageable search problem. For simple cases, the global minimum of the resulting objective function can be determined through use of a variety of search techniques. Reduced parameterizations have the additional benefit of being physically realizable. Long cables with arbitrary sensor spacings have the potential to be difficult to manufacture; by limiting the choice of geometries we are implicitly adding a side constraint with possible cost benefits.

In this preliminary investigation, we use our optimal experiment design algorithm to improve the configuration of active seismic monitoring systems within a crosswell geometry. We first consider a two parameter array design problem and explore the characteristics of the quality metric. We compare the convergence and performance of two optimization methods, the Nelder-Mead downhill simplex and multilevel coordinate search strategies for selecting array geometries. For this simple example, both techniques converge to the globally optimal design. We also consider a more com-

plicated four parameter design problem which optimizes a combination of array length and vertical offset. We conclude by examining trade-offs between source sparsity and the quality of tomographic reconstructions. Preliminary results suggest that high-quality differential images can be generated using only a small number of optimally positioned sources.

PRINCIPLES & PREVIOUS RESEARCH

As mentioned previously, optimal designed algorithms can be roughly decomposed into three components, the metric used to discern an "optimal" experiment, the space of experiments considered as possible solutions, and the search technique used to find the best design. Another important component which we will only briefly cover is the implementation of secondary constraints, either direct limitations on the geometry or auxiliary parameters such as survey cost, acquisition time etc. In this section we will outline a framework for expressing optimal design search problems and their associated components.

A Notation For the Optimal Design Problem

Implicit in the entire design process is the inversion step itself, i.e. the methodology by which measurements are transformed into estimates of earth properties. Most optimal design algorithms are formally posed within the framework of linear inverse problems, sometimes with ad-hoc extensions to the non-linear case. We will use the traditional notation for such problems (Menke, 1984),

$$\mathbf{Gm} = \mathbf{d}, \tag{1}$$

where $\mathbf{G}$, referred to as the kernel, maps a model ($\mathbf{m}$) to a dataset ($\mathbf{d}$). $\mathbf{G}$ encapsulates both

the operative physics and the geometry of the experiment. Linear inversion attempts to undo the action of $\mathbf{G}$ thereby reconstructing an earth model given a dataset.

As mentioned previously, $\mathbf{G}$ contains an implicit dependence on the experiment geometry; since we are searching across these possible geometries this relationship must be written explicitly. Let the geometry of our permanent source/receiver array be encapsulated by a vector ξ. In the most general case where we are free to locate each of d sources and e receivers at any point in space we express the experiment geometry as,

$$\xi \;=\; [\mathbf{s}_1, \mathbf{s}_2, ...\mathbf{s}_d : \mathbf{r}_1, \mathbf{r}_2, ...\mathbf{r}_e] \tag{2}$$

where $\mathbf{s}$ and $\mathbf{r}$ are source and receiver locations in the appropriate number of spatial dimensions. In 3D, the number of scalar design parameters in the experiment becomes $(d+e)\times 3$. The optimality metric, Ω, maps ξ to a scalar measure of experiment quality. The optimal design geometry, ξ_{optim} can then be written as:

$$\xi_{optim} \;=\; min(\Omega(\xi, \{\alpha_1, ...\alpha_t\})), \tag{3}$$

where the set of α variables are auxiliary parameters which are required to evaluate Ω but are not part of the search problem. An example of α would be a background velocity model required to calculate $\mathbf{G}$. The metric Ω can be further decomposed into two parts, a raw measure of experiment quality (Ω_u) and a set of f soft secondary constraints (Ω_{c_f}), possibly including information pertaining to spatial limitations of the survey, field costs, or acquisition time. Momentarily dropping

the arguments to Ω, we can write this decomposition as,

$$\Omega \;=\; \Omega_u + \sum_{i=1}^{f} \beta_i \Omega_{c_i}, \tag{4}$$

where β_i is a weighting factor which scales the strength of the ith soft constraint terms. Equation 4 is in no way encompassing since the constraint term can also be implemented in a "hard" form as part of the search algorithm itself. This notation for writing Ω is not well-suited to expressing greedy design algorithms for which the dimensions of ξ vary dynamically as part of the search process.

Previous Research

Despite some successes, existing optimal design algorithms suffer from a combination of problems, mainly inappropriate choices for Ω, the experiment quality metric, and/or poor parameterizations for the geometry search space, typically involving the explicit use of ξ. A bad choice of Ω or ξ can in turn result in an unnecessarily large search space with non-ideal properties, particularly the existence of extraneous local minima.

Experiment Quality Metrics

The quality metrics proposed by previous authors roughly fall into two camps, those who define quality in terms of the eigen-properties of a given design (Barth and Wunsch, 1990; Curtis and Snieder, 1997; Curtis, 1999a,b) and more applied practitioners who optimize heuristic attributes such as fold or ray coverage (Liner et al., 1999; Vermeer, 2003; Galbraith, 2004). Design algorithms based on SVD analysis of the linear inverse problem were pioneered in a geophysical context by

Maurer and Boerner (1998) and Curtis (1999a) who adapted previous work by Barth and Wunsch (1990) and earlier authors (Box and Lucas, 1959; John and Draper, 1975). All of these techniques seek to maximize the amount of information contained within a given geophysical survey, typically by reducing the linear problem's null space. Curtis (1999b) provides a catalog of five experiment quality metrics based only on the eigenspectrum of $\mathbf{G}$. Most of these metrics involve sums or products of eigenvalues, possibly truncated so as to consider only values above or below a given threshold.

Despite their apparent elegance, global SVD based techniques suffer from several clear weaknesses. Methods which rely solely on examination of the eigenspectrum provide no avenue for incorporating zones of interest since all spatial information is encoded in the right eigenvectors; the resulting designs often optimize the experiment to recover properties within unimportant portions of model space. This is particularly problematic in the case of monitoring experiments where we have prior knowledge of regions where change might occur. Curtis (1999b) attempts to remedy this problem by incorporating a second "focused" component of Ω by examining projections of model regions onto the right singular vectors.

An attractive set of related quality metrics are those which make direct use of the model resolution matrix, $\mathbf{R}$, which for linear problems maps the true model ($\mathbf{m}_{true}$) to the estimated model ($\mathbf{m}_{est}$) i.e. $\mathbf{m}_{est} = \mathbf{R}\,\mathbf{m}_{true}$. In the case where $\mathbf{R} = \mathbf{I}$, the true model is perfectly reconstructed. Routh et al. (2005) suggests a computationally feasible approach for sequentially reconstructing the kth row of $\mathbf{R}$ by solving for point-spread functions. Routh et al. (2005) then uses the spatial compactness of the point-spread functions to estimate the suitability of experiment

designs yielding a quality metric of the form,

$$\Omega_u(\xi) \;=\; \|\mathbf{Q}_k(\mathbf{p}_k(\xi) - \Delta_k)\|_2^2, \tag{5}$$

where $\mathbf{p}_k$, the point-spread response, is the solution of a regularized linear inverse problem of the form

$$\begin{bmatrix} \mathbf{G}(\xi) \\ \lambda \mathbf{W}_m \end{bmatrix} \mathbf{p}_k \;=\; \begin{bmatrix} \mathbf{G}(\xi)\boldsymbol{\Delta}_k \\ 0 \end{bmatrix} \tag{6}$$

In equation 6, $\mathbf{W}_m$ is a model-space regularization operator ($\mathbf{I}$ in the case of damping) and $\boldsymbol{\Delta}_k$ is an impulse function in the model domain; the product $\mathbf{G}\boldsymbol{\Delta}_k$ is the synthetic data which would be generated by such an impulse. Equation 5 also includes a weighting operator $\mathbf{Q}_k$ which penalizes elements of $\mathbf{p}_k$ away from the kth cell according to a specified distance function (see Routh et al. (2005) for an explicit formulation). In words, Routh's point-spread metric measures how closely (in an l_2 sense) a given geometry can reconstruct a delta feature at some location in the model. This provides a tempting alternative to SVD techniques since it requires only an least-squares inversion routine and can take full advantage of sparse solvers. Because regularization can be easily incorporated into the point-spread calculation, the effect of prior smoothness constraints on the optimal geometry can also be evaluated. A final more conceptual benefit is that metric 5 truly operates on the inverted model; the benefits of improving Ω are easily visible in the resulting images.

The limitation of Routh's point-spread metric as written in equation 5 is that the resolution is only evaluated at a single location k; to evaluate such a metric over a larger zone of interest would

require a full inversion for each cell within this region. As we will discuss in the following sections, we adopt a metric similar to equation 5 except that we replace $\mathbf{\Delta}_k$ with a single or small suite of models with broader (although less precise) features.

A second class of techniques uses easily computed metrics which provide a more heuristic guide to experiment quality e.g. common-midpoint fold, azimuthal coverage, ray density, or more general measures of operator sensitivity. One example of this type of approach is the work of Liner et al. (1999) who use a mix of soft and hard constraints to search for survey geometries which satisfy acquisition criterion including common-midpoint fold and maximum offset. The resulting quality metric is very inexpensive to evaluate; millions of survey geometries can be tested for suitability in a relatively short period of time. Unfortunately, such metrics have several well-known problems, the most crucial is that they can be fulfilled even in cases where the resulting surveys have deficiencies from an inversion perspective (see Curtis and Snieder (1997) for the equivalent issue in the dual problem of mesh design).

Parameterizing Survey Geometry

Almost as important as the selection of a quality metric is the set of geometries considered as valid surveys since this determines the dimensions of the required search space. Assuming a fixed number of sources and receivers, the most flexible possible representation is the vector ξ which allows arbitrary positions for all d sources and e receivers; this results in a problem of dimension $(d+e)\times 3$. In some cases such as when the sensors are constrained to a surface (Barth and Wunsch, 1990) or a line (Curtis, 1999a), each source and receiver has less than 3 degrees of freedom thereby slightly reducing the search space. However, even for mid-sized seismic surveys $(d+e)$ inevitably becomes

quite large, particularly in the context of global search techniques. The resulting optimization problem may exhibit several unattractive attributes, primarily the existence of numerous local minima in the objective function. Additionally, the optimal geometries are often difficult to realize in practice; most acquisition techniques rely on some degree of regularity and the custom fabrication of take-out cables or streamers with arbitrary sensor spacings can be prohibitively expensive.

COMBINING PARSIMONIOUS GEOMETRY REPRESENTATIONS & IMAGE-BASED QUALITY METRICS

Our approach to the survey design problems combines a parsimonious parameterization of survey geometry with an image-based survey quality metric similar to the point-spread metric advocated by Routh et al. (2005). The resulting optimization problem is solved using one of two direct search methods, either the local Nelder-Mead downhill simplex algorithm (Nelder and Mead, 1965) or the global Multilevel Coordinate Search algorithm developed by Huyer and Neumaier (1999). This blend of a reduced search space, an intuitive model domain quality metric, and robust search algorithms results in a method which both scales to mid-sized problems and significantly improves the spatial resolution of the resulting experiments.

As mentioned previously, an alternative to searching across all possible geometries is to introduce a limited subset of feasible configurations described by a second set of parameters. In this case, we have an operator Φ which maps a short vector $\mathbf{q}$ to a full geometry i.e. $\Phi(\mathbf{q}) = \xi$. The elements of $\mathbf{q}$ are typically a small number of geometry descriptors e.g. array length, array center location, line spacing etc. While the mapping function Φ is designed to produce reasonable geometries, some constraints must still be applied to the elements of $\mathbf{q}$ necessitating a penalty function of the form,

$\Omega_c(\mathbf{q})$

The resulting problem minimizes the combined Ω with respect to $\mathbf{q}$,

$$\xi_{optim} \;=\; min(\Omega_u(\Phi(\mathbf{q})) + \sum_{i=1}^{f} \beta_i \Omega_{c_i}(\mathbf{q}_i)) \tag{7}$$

While the global minimum of Ω with respect to ξ is not guaranteed to be located in the lower dimensional space covered by Φ, the geometry produced by optimizing $\Phi(\mathbf{q})$ will typically be better than an arbitrary configuration and will hopefully be easy to physically construct if the parameterization $\mathbf{q}$ is chosen correctly. Since $\mathbf{q}$ is of a small dimension, searching for a quasi-optimal Ω is an achievable task. As will be shown in later sections, the resulting objective function can be unimodal for design problems with a low number of dimensions making it amenable to local search techniques. This approach to designing surveys by optimizing a limited set of parameters describing geometry is intuitive to those familiar with large-scale seismic acquisition; Liner et al. (1999), Morrice et al. (2001), Vermeer (2003), and others have posed their survey design algorithms in terms of similar parameters such as line offset and shot density instead of arbitrary locations for each geophone or source.

Up to this point we have not mentioned our formulation for the raw experiment quality metric (Ω_u). In our case, Ω_u will be a measure of a given geometry's ability to reconstruct a known test model, $\mathbf{m}_{true}$, i.e.

$$\Omega_u(\Phi(\mathbf{q})) \;=\; \|\mathbf{m}_{true} - \mathbf{m}_{est}\|_2^2 \tag{8}$$

The estimated model, $\mathbf{m}_{est}$, is calculated by solving a regularized least-squares problem of the form,

$$\begin{bmatrix} \mathbf{G}(\mathbf{m}_{base}, \Phi(\mathbf{q})) \\ \lambda_x \mathbf{D}_x \\ \lambda_z \mathbf{D}_z \end{bmatrix} \mathbf{m}_{est} = \begin{bmatrix} \mathbf{d} \\ 0 \\ 0 \end{bmatrix}. \tag{9}$$

$\mathbf{G}$, as written in equation 9, depends on a prior model estimate, $\mathbf{m}_{base}$ around which we linearize the problem. $\mathbf{m}_{base}$ and $\mathbf{m}_{true}$ are not the same; $\mathbf{m}_{base}$ is a reference model used for calculating $\mathbf{G}$ while $\mathbf{m}_{true}$ is the true model used for generating linear synthetic data and evaluating the quality metric. Note that "true" in this case denotes a known hypothetical model used for testing purposes rather than a measured perturbation; this is because the design process should be performed before installation of the monitoring system and hence before any data is available on the time-lapse process. $\mathbf{D}_x$ and $\mathbf{D}_z$ are 1st order derivative operators in the x and z directions while λ_x and λ_z are the associated regularization parameters. Since the background model is known, the $\mathbf{d}$ in equation 9 is the evaluation of a linear forward problem on the current geometry with the addition of noise i.e. $\mathbf{d} = \mathbf{G}(m_{base}, \Phi(\mathbf{q}))\, \mathbf{m}_{true} + \mathbf{d}_{noise}$. Additionally, we write the problem in terms of x and z only because we are considering the 2.5 dimensional imaging problem; the extension of the formulation to three dimensions (y) is straightforward.

The regularization matrices included in equation 9 are clearly not restricted to derivatives; ideally, the regularization operator should be tailored to match prior knowledge of the process being monitored (Ajo-Franklin et al., 2007b) but in this case we choose derivatives for the purpose of simplicity. The operator choice and strength will also introduce bias into the optimal design. We typically select fixed regularization parameters using the discrepancy method applied to a preliminary geometry since in the design process our noise levels are known; in reality the magnitude

of λ_x and λ_z or even the style of the regularization operator could be considered part of the design process since field noise levels are difficult to ascertain prior to deployment.

An important component of the inversion quality metric shown in equation 8 is the choice of test model, $\mathbf{m}_{true}$. As mentioned previously, the point-spread approach uses a model with a delta spike at a single location. While point spread functions are an excellent local measure of resolution, it requires a large number of independent evaluations to assess resolving power over an extended model region. An alternative is to use a single or small group of models which provide information on resolution for a larger region which includes the imaging target. One such commonly used metric in the global tomography community is the checkerboard test where resolution is evaluated by looking at the smearing of a regular array of features. Checkerboard tests cannot recover the same resolution information as a series of point-spread evaluations since the smeared components of different features may overlap. In our quality metric, $\mathbf{m}_{true}$ is typically either the product of a checkerboard and a localized window function which is only positive in the target region as is shown in figure 1 or an anomaly constructed from multiphase flow modeling results.

[Figure 1 about here.]

For monitoring applications, spatial localization is desirable since the perturbed region is often confined to a single geological unit. This is particularly true in cases where the process being monitored is a fluid injection (e.g. CO_2, bio-stimulant fluid, steam) and geophysical measurements are being used to delineate the shape and extent of "fronts" in the flooding process. While checkerboard tests are not the ideal test of survey resolution, as discussed in Leveque et al. (1993), they are relatively inexpensive to perform, a key attribute when used in the inner portion of an objective function evaluated as many as 10^6 times. Ideally, image metrics like equation 8 would be evalu-

ated for a suite of models related to the process being monitored as we will consider in one of our examples for the specific case of multiphase flow involving supercritical CO_2 .

From a computational perspective, the quality metric shown in equation 8 requires two main operations, the generation of the forward operator given the background model and the solution of a regularized linear inverse problem to generate the $\mathbf{m}_{est}$. Since both of these components are available as part of standard imaging packages, this process often requires minimal code modification on the part of the user. Evaluation of equation 8 can also be performed without the explicit construction of any of the operators making it useful in cases where only the actions of $\mathbf{G}$ and $\mathbf{G}^T$ on vectors can be performed in core memory.

Design Optimization : Two Algorithms

To this point, we have described a simple system for exploring experimental designs which combines an l_2 image reconstruction metric and a parsimonious description of experiment geometry. The resulting objective functions are well-behaved for several common seismic array design parameters although this observation almost certainly does not generalize to arbitrary parameterizations (or geophysical problems).

Since the selection of an algorithm for minimizing the right hand side of equation 7 strongly depends on the character of the objective function, we should summarize in advance some observations, some of which can be inferred from our later examples. First among these attributes is the dimensionality of the objective function; using a parsimonious geometry description guarantees a low-dimensional objective function by design. Crucially, the objective function is also expensive to evaluate. While our l_2 image metric can scale efficiently to large problems, it is still expensive,

requiring at the very least a forward solve and a full inversion. Another attribute key to selecting an optimization technique is the lack of analytic forms for the gradient of the objective function with respect to the design parameters. Additionally, for all but the simplest choice of parametrizations the design objective function should have multiple local minima; however, for the problems we have been able to explore visually (2 variables) the objective function surface is often dominated by a single broad minimum. A related observation is that the objective function surface seems relatively smooth; for our tomographic monitoring problem, particularly when appropriately regularized, we do not typically observe sudden jumps in image quality due to small perturbations in experiment geometry. The character of such surfaces, visible for 2 parameter problems, is that they are dominated by broad plains with the occasional valley. While some possible designs are, in fact, very bad, large regions of parameter space often exhibit similar l_2 image quality metrics. The objective function surface for these regions is correspondingly flat. In some cases, valleys exist, indicating trade-offs between multiple design parameters.

Previous optimal experiment design studies have made extensive use of stochastic global search methods, with genetic algorithms (Curtis, 1999a), and simulated annealing (Barth and Wunsch, 1990) being the most popular techniques. We examine two alternative derivative-free approaches to minimizing the design metric, the downhill simplex method developed by Nelder and Mead (Nelder and Mead, 1965) and the Multilevel Coordinate Search algorithm (Huyer and Neumaier, 1999). Both methods are deterministic in contrast to the stochastic algorithms often used in the design literature. The Nelder-Mead method is intrinsically local while Multilevel Coordinate Search attempts to balance local and global search goals with guaranteed (but very slow) convergence even in the case of multi-modal objective functions.

The Nelder-Mead algorithm is a popular (Press et al., 1992) local search approach which in at least one previous case (Muzic et al., 1996) has been successfully applied to experiment design. The Nelder-Mead algorithm does not compute numerical derivatives using finite-differences; instead, the objective function is evaluated at a set $n+1$ points (referred to as a *simplex*), where n is the dimension of the optimization problem, and this set is sequentially altered by a series of heuristic rules (see Press et al. (1992) for details and a simple implementation). In practice, the algorithm reliably creeps to a local minimum of the objective function. As with any local method, the Nelder-Mead algorithm converges to the local minimum closest to the starting location making it susceptible to multi-modal objective functions.

The Multilevel Coordinate Search algorithm, descended from the DIRECT method proposed by Jones et al. (1993), is a deterministic global search algorithm which attempts to balance large scale exploration of the parameter space with local refinement in regions with promising objective function values. The Multilevel Coordinate Search algorithm is guaranteed to converge to a global minimum assuming the objective function is continuous in the vicinity of the minimum; unfortunately the convergence bound is weak in the sense that an exponential number of steps might be required. The search process is initialized with a hyper-box bounding all of the control parameters thus allowing implicit incorporation of hard bounds on design parameters. This box is then subjected to different sub-division and sampling operations; the method of division cycles between global and local refinement steps. The original comparison of Huyer and Neumaier (1999) suggests that this multilevel search approach outperforms most deterministic global search algorithms for the suite of test functions proposed by Dixon and Szego (1978).

APPLICATION TO THE SEISMIC MONITORING PROBLEM

Our discussion of experiment design so far has been general with no assumptions regarding the operation which $\mathbf{G}$ performs, the model parametrization represented by $\mathbf{m}$, or the type of data stored as $\mathbf{d}$. We will now apply our formulation to the specific example of differential seismic traveltime tomography, a technique being used as part of several integrated seismic monitoring projects. All examples which will be shown use a crosswell geometry to match field deployments in which we are currently participating in.

In the case of differential inversion we consider two datasets, $\mathbf{d}_1$ and $\mathbf{d}_2$, acquired at different times, but with the same geometry. Instead of inverting the two datasets independently, differential tomography inverts $\Delta\mathbf{d}$, the difference between measurements made at time 1 and time 2, for $\Delta\mathbf{m}$, the temporal perturbation in model parameters. In our case, $\Delta\mathbf{d}$ is the relative traveltime difference between two different surveys for the same source/receiver pair while $\Delta\mathbf{m}$ is a perturbation in slowness. $\mathbf{G}$ is the ray-theoretic forward modeling operator. The model is defined on a rectilinear mesh of constant slowness cells. Differential imaging approaches can be problematic in cases where the dominant changes in delay time are due to localized effects near the sources or receivers which are not the target of the monitoring experiment e.g. water table variations or seawater temperature changes (Vesnaver et al., 2003) in the case of timelapse surface reflection surveys. However, deep boreholes are relatively stable environments and semi-permanent arrays offer an almost ideal scenario where changes in formation coupling are minimized.

We treat the differential tomography problem as a linear perturbation; we assume that a background velocity model, $\mathbf{m}_{base}$, is available and calculate curved ray-paths in that initial model. Recovery of $\Delta\mathbf{m}$ is then considered as a purely linear inverse problem. This simplification seems

reasonable in the case of seismic monitoring since the property changes induced by human perturbations are often (but not always) considerably smaller than background variations. Unlike the static imaging problem where the earth model is initially unknown, most monitoring surveys have access to background property estimates from reconnaissance/exploration surveys or well logs.

Our optimal experiment design algorithm is designed to find surveys which optimally recover $\Delta\mathbf{m}_{true}$ given $\mathbf{m}_{base}$ and constraints on the locations of elements in ξ. In this approach, the experiment is not designed to optimally image the background model but only to resolve a localized perturbation. As discussed in the previous section, $\Delta\mathbf{m}_{true}$ will in our case be either a spatially limited checkerboard model or the results of an anomaly generated from a flow modeling run specific to the site in question.

Evaluation of Ω for a given $\mathbf{m}_{base}$, $\mathbf{q}$, and mapping function can be written in pseudo-code as:

1. Map the reduced parameter set, $\mathbf{q}$, to the full geometry ξ using Φ;
2. Generate $\mathbf{G}$ for the geometry ξ in $\mathbf{m}_{base}$, a non-linear forward modeling step;
3. Calculate a perturbed synthetic dataset using the $\mathbf{G}$ from the background model, $\Delta\mathbf{d} = \mathbf{G}\,\Delta\mathbf{m}_{true}$;
4. Invert $\Delta\mathbf{d}$ for $\Delta\mathbf{m}_{est}$ using a regularized linear solver;
5. Evaluate the image quality objective function, $\Omega_u = \|\Delta\mathbf{m}_{est} - \Delta\mathbf{m}_{true}\|_2^2$;
6. Evaluate the geometry penalty function Ω_c on ξ;
7. Compute the combined experiment quality metric, $\Omega = \Omega_u + \Omega_c$.

We calculate $\mathbf{G}$, the forward modeling operator, in a 2.5 dimensional geometry designed to accommodate heterogeneous 2D structure and well trajectories with out-of-plane deviations. The solution to the eikonal equation is calculated using a finite-difference eikonal solver (Vidale, 1988; Sethian and Popovici, 1999); we took advantage of components in the FAST package developed by Zelt (Hole and Zelt, 1995). Frechet derivatives are extracted using reverse ray-tracing (Aldridge and Oldenburg, 1993) in the shot-domain. The regularized linear inversion in step 4 is performed using the LSQR algorithm developed by Paige and Saunders (1982) and solves equation 9. The geometry penalty function mentioned in step 6 is simply a barrier term which evaluates to zero within the interior of the modeling domain and smoothly increases to a large value as source and receiver approach the edges. Ω is optimized over the reduced vector $\mathbf{q}$ using either the Nelder-Mead or Multilevel Coordinate Search algorithm as discussed previously.

In practice, both the assumptions of prior background structure and monitoring linearity can be clearly violated. In cases where $\mathbf{m}_{base}$ is grossly inaccurate, the resulting survey design may not have equivalent performance, particularly in situations where significant ray bending is induced by the unknown feature such as a strong low velocity zone. Similarly, in some situations the model perturbation, $\Delta\mathbf{m}$, might also be large enough to cause significant changes in ray paths; this also brings into question the validity of differential measurements since $\mathbf{d}_1$ and $\mathbf{d}_2$ will have sampled different zones in the subsurface. In this case, the previously discussed metric for experiment quality might still have utility but the entire problem must be shifted so that both baseline and repeat datasets are inverted using a non-linear approach.

Designing an Optimal Asymmetric Crosswell Array

A complete test of our optimal design algorithm was performed as part of a retrospective examination of the Frio crosswell seismic monitoring installation. The Frio demonstration project (Hovorka et al., 2006) was a broad multi-institutional effort to improve understanding of the *in situ* dynamics of super-critical CO_2 injection within a saline aquifer located in East Texas. Motivated by previous seismic monitoring experiments targeting CO_2 floods (Lazaratos and Marion, 1997), Lawrence Berkeley National Laboratory carried out imaging experiments during both the first and second phases of the Frio project. The first experiment consisted of a pair of traditional time-lapse crosswell surveys where both sources and receivers were deployed via wireline (Daley et al., 2005). While the wireline surveys successfully imaged the expanding CO_2 plume as shown by Daley et al. (2007a) and Ajo-Franklin et al. (2007b), the existence of only a single repeat survey made evaluation of flow dynamics difficult.

The second Frio seismic imaging experiment evaluated the combination of a single permanently installed downhole piezoelectric source and a fixed array of 24 hydrophones with both devices deployed on production tubing (Daley et al., 2007b). This experiment clearly demonstrated the high level of repeatability possible with a permanent monitoring system. More importantly, the acquisition of datasets over time intervals as short as 15 minutes allowed real-time monitoring of the seismic signal during the injection process. However, the use of only a single source prevented the Frio II seismic experiment from effectively imaging CO_2 movement although qualitative information on plume geometry was obtained.

Future monitoring experiments are expected to move beyond the single-source geometry used in the Frio II trial and combine continuous monitoring with a multi-source geometry more suitable for

tomographic reconstruction. Considering the high cost of each additional source transducer in comparison to hydrophone pods, an asymmetric source/receiver distribution seems almost inevitable. This combination of high capital cost and minimal previous experience with similar acquisition systems makes this particular design problem a perfect candidate for optimal experiment design techniques.

A Two Parameter Design Problem

For our first example, we will consider a simple crosswell array optimization problem where the geometry is fully described by two parameters, the vertical extents of the source and receiver arrays. In this case $\mathbf{q}$, the reduced parameterization is simply $[P_1, P_2]$. Figure 2 shows the intended geometry. Both the source and receiver arrays are centered around a single 5 m target layer with an alternating pattern of 1.5 m wide perturbations. All figures are plotted in terms of array 1/2 widths i.e. the distance from the array center to the top of the array. In order to provide insight into the design challenges at the Frio site, we selected an asymmetric geometry distribution with 8 sources and 80 receivers. Each inversion calculated as part of evaluation of the quality metric was performed on a 75 x 210 sample mesh yielding a underdetermined 640 x 15,750 (data x model) problem. The synthetic differential traveltime data used in each sub-inversion was contaminated with 0.5% zero mean gaussian noise. The discrepancy method, applied to the inverse problem generated by the initial source/receiver geometry, was used to determine an optimal isotropic regularization parameter ($\lambda_x = \lambda_z$ in equation 9).

[Figure 2 about here.]

Considering the low dimensionality of the search problem, we first directly evaluated the experiment quality metric on a regular 2D grid to gain some insight into the optimization problem and the corresponding survey geometries. The existence of a calculated reference surface also allows us to examine the convergence properties of both our global and local search schemes. Figure 3 shows the image quality metric for array 1/2 width values between 2 and 16 meters. As can be seen, the objective function surface is relatively well behaved with a localized trough-like minimum corresponding to source array 1/2 widths near 6 meters. The global minimum occurs on the domain boundary at close to the maximum receiver array width.

[Figure 3 about here.]

Figure 4 illustrates the linkage between the experiment quality surface and the actual inversion results. While the top panel shows the quality surface, the bottom row shows the true reference checkerboard model [A] and tomographic images corresponding to 3 geometries sampled by the grid search. Panel [B] shows a narrow aperture geometry where the sources and receiver arrays are localized near the zone of interest. Panel [C] shows the geometry and tomogram associated with the global minimum; this "optimal" solution couples a source array of moderate length to a wide receiver array. Panel [D] depicts the result corresponding to a wide angular aperture in both the source and receiver wells. As can be clearly seen, the optimal geometry successfully resolves checkerboard cells near both wells with only a small amount of smearing visible above and below the target zone. In contrast, the narrow aperture geometry tends to smear features along the primary survey diagonals imparting an "X" shaped overprint on the tomogram. The maximum aperture geometry cannot resolve features near the source well due to sparse vertical spacing. This result is significant since it suggests that asymmetry in the number of sources and receivers can be

partially compensated for by appropriately adjusting array lengths in cases where the target zone is spatially limited.

[Figure 4 about here.]

Figure 5 compares the convergence of the Nelder-Mead (top) and Multilevel Coordinate Search (bottom) algorithms when applied to the same test case. In each panel, the background color map is derived from the grid evaluation while the superimposed symbols indicate where each algorithm evaluated the objective function. Both algorithms converge to the correct global minimum as estimated by the original grid search. Given this particular start location (shown as a red circle), the Nelder-Mead solver converged to within tolerance after 130 evaluations of the objective function. The Multilevel Coordinate Search solver was initialized with only the bounds on the domain but required 203 evaluations to achieve the same level of accuracy.

Figure 5 also gives insight into the evaluation patterns of the two algorithms. Nelder-Mead, as with most local search methods, "feels" out the trough in the objective function and does not sample locations outside of this zone of influence. In cases where multiple local minima were present, this behavior would guarantee that Nelder-Mead would be sensitive to start location. In contrast, Multilevel Coordinate Search samples the objective function at several locations outside the trough in zones with significantly worse quality metrics. The method's search heuristic attempts to balance global and local search performance by cycling through different types of sub-sampling patterns; in this case, after some initial linear sampling steps, the algorithm focused on the region containing the global minimum.

[Figure 5 about here.]

A Four Parameter Design Problem

While the first test problem provided insight into the simplest class of crosswell array designs, we decided to investigate a higher dimensional problem with more utility to sites similar to Frio. The primary injection unit at Frio is located within relatively close proximity to a salt dome; upward movement of the salt has resulted in faulting near the flank and has imparted an upward dip of about 17^o to the target layer. We expected that this significant dip in the target would necessitate vertical re-positioning of the arrays in addition to adjustments in array width. Figure 6 shows this slightly more complicated geometry; $\mathbf{q}$ is now a vector of length 4 including the center depths of the source (P_1) and receiver (P_2) arrays in addition to the source and receiver array 1/2 widths (P_3, P_4).

[Figure 6 about here.]

Preliminary numerical tests indicated that the Nelder-Mead algorithm, when applied to this design problem, showed significant sensitivity to starting location; based on this observation we focused on application of the Multilevel Coordinate Search method. Panel [A] of figure 7 shows the test checkerboard model with a dip of 17^o to match the injection unit at Frio. Panel [B] depicts the tomographic results for an initial "best guess" geometry where the source and receiver arrays effectively encompassed the target region. Panel [C] shows the optimal geometry as determined by Multilevel Coordinate Search. In this case, convergence occurred after 333 objective function evaluations. Since only the 4D bounds on $\mathbf{q}$ are required for the search algorithms, panel [B] is included purely for the purpose of illustration.

[Figure 7 about here.]

The optimal geometry shown in figure 7 exhibits several interesting attributes. As in the previous example, the optimal design has improved spatial resolution near the source well and reduces artifacts above and below the imaging target. The magnitude of the checkerboard features are also closer to the true model with less shape distortion visible in the high velocity zones. Like the two parameter case, the best design has asymmetric source and receiver array widths. Additionally, the source array is shifted upwards so as to shoot across the dip of the target layer.

A Realistic Flow-Based Test Problem

The first and second examples shown assumed both a homogeneous background velocity for $\mathbf{m}_{base}$ and a spatially limited checkerboard model for the image quality test model for $\Delta\mathbf{m}_{true}$. As mentioned previously, the background model should ideally incorporate prior knowledge of velocity structure while the image quality test model should present a geometry and magnitude representative of the physical process being monitored. In the case of the Frio pilot experiment, both components are available; velocity structure from sonic logs and perturbation estimates from preliminary multi-phase flow modelling results. In this example, we incorporate this additional data into our experiment design approach and evaluate the performance of the resulting algorithm.

[Figure 8 about here.]

Panel [A] of figure 8 depicts a background velocity model derived from 2D extrapolation of logs acquired in the Frio injection well with a local dip determined from gamma ties. The units included are members of the Blue Sand interval, the target of the Frio II seismic monitoring experiment discussed in Daley et al. (2007b). Only velocity variations within the target unit used for flow modeling were included; the flow model used a closed boundary for the shale units above and

below the Blue Sand. Core porosity and permeability measurements were also much more numerous within the Blue Sand, thus allowing providing better constraints on the rock-physics approach used for later fluid substitution steps. V_p values are relatively low, ranging from 2650 to 2765 m/s with a background velocity of 2700 m/s used for zones outside the Blue Sand. The depths show in panel [A] are in a local coordinate frame; the absolute wireline depth of the target unit is aproximately 1650 m below surface. In this test case, the velocity model shown in panel [A] of figure 8 was used for $\mathbf{m}_{base}$; although the quality metric evaluation only involves a linear inversion step to recover $\Delta\mathbf{m}_{true}$, the true (curved) ray-paths through $\mathbf{m}_{base}$ were used for the inversion. However, since the velocity variations within the background model were relatively small, only a small number of ray-paths exhibited significant bending, in particular rays traveling at shallow angle impinging on the high velocity zones at the top and bottom of the reservoir unit. Also shown in panel [A] are the injection well (left vertical line) and the monitoring well (right vertical line) with the true lateral offset seen at the Frio site (30 m).

As part of retrospective analysis of the Frio II experiment described in Ajo-Franklin et al. (2007a) and Daley et al. (2008), a series of refined flow models were created, constrained by core permeability/porosity measurements, injection mass, CO_2 break-through times, and continuously acquired seismic data. 3D multi-phase flow modeling was then performed using the TOUGH2/ECO2N system (Pruess and Spycher, 2007). The purpose of the original flow modeling exercise was to understand variations in lateral permeability structure at Frio but in this example we will co-opt them to generate a realistic velocity perturbation for use in experiment design.

To obtain a $\Delta\mathbf{m}_{true}$ to use as a substitute for the checkerboards described previously, a single time-frame of CO_2 saturation was transformed into a model of V_p. Fluid properties were determined

for *in situ* temperatures and pressures using standard thermophysical property estimates for CO_2 (Lemmon et al., 2005) and the brine properties predicted by the model of Batzle and Wang (1992). Elastic property changes induced by the CO_2 plume were estimated using White's patchy saturation model (White, 1975) as modified by Dutta and Ode (1979). Panel [B] of figure 8 shows the predicted perturbation in V_p due to CO_2 injection. As would be expected, since the *in situ* density of CO_2 is approximately 700 kg/m^3, considerably lighter than brine, the plume primarily migrates up-dip towards the monitoring well. The maximum velocity change seen in the CO_2 plume is less then that observed in the field, approximately -350 m/s in contrast to variations of over -500 m/s seen in the Frio C Sand during the Frio I crosswell experiment (Daley et al., 2007a); this is probably due to inadequacies in the rock-physics model used for fluid substitution. However, since we are only considering the linearized design problem (the plume does not alter ray-paths), this discrepancy in magnitude will not have a significant impact on the resulting designs. One interesting characteristic of the plume is a vertical kink visible near 22 m offset which resulted from incorporation of lateral permeability variations in the original flow model. This feature is a key small-scale imaging target which might be difficult to resolve using timelapse tomography.

For this test, we consider asymmetric source/receiver geometries with 6 sources, 48 receivers and 4 degrees of design freedom; like the previous example we are searching for the optimal array offsets and lengths to image $\Delta\mathbf{m}_{true}$. Each inversion calculated as part of evaluation of the quality metric was performed on a 176 x 217 sample mesh (0.3 m spacing) yielding an underdetermined 288 x 38,192 (data x model) problem. The synthetic differential traveltime data used in each sub-inversion was contaminated with 0.5% zero mean gaussian noise. The discrepancy method applied to the initial source/receiver geometry was used to determine an optimal isotropic regularization parameter. The design guess ($\mathbf{q}_{init}$) in this case included arrays centered around the plume at

depths of 35 m with large initial apertures of 46 m. Like the previous 4 parameter optimization problem, experiments with the Nelder-Mead simplex algorithm failed to converge hence we used the Multilevel Coordinate Search algorithm for all final tests.

[Figure 9 about here.]

Figure 9 shows the true velocity model perturbation used as the test perturbation in panel [A], the inversion result for the initial geometry guess in panel [B], and the differential tomogram generated by the optimal geometry in panel [C]. Although the initial guess does a reasonable job of resolving the plume, yielding the correct dip and termination points, the optimal geometry successfully delineates both the small vertical kink near the center of the plume and the structure of the plume near the source well. From a quantitative perspective, the l_2 quality metrics (Ω_u) of the initial and optimal geometries are 0.0011 and 0.00077 respectively. The Multilevel Coordinate Search algorithm required 622 iterations to converge to the optimal design. Much like previous solutions, the optimal geometry incorporated asymmetric array lengths with the source array considerably shorter than the receiver array. In this case, the optimal design did not exhibit the "cross-dip" shooting direction seen in example 2, possibly because of the limited lateral resolution required to image structure within the plume.

A relevant question when considering the optimization of survey geometries is the sensitivities of designs to $\mathbf{m}_{base}$, which could be inaccurate, even in regions with good well control. Since our best estimate of $\mathbf{m}_{base}$ in the prior case did not exhibit large velocity contrasts, the design would differ only minimally from the case where a homogeneous model was used for the background. To explore the role of higher velocity contrasts in the background model, we scaled the perturbations present in $\mathbf{m}_{base}$ by a factor of four to yield a model with the same layered structure but velocity variations

between 2522 m/s and 3073 m/s over short spatial scales within the reservoir unit. The resulting $\mathbf{m}_{base}$ generated strong ray bending, particularly in the vicinity of the low velocity channel. Using this scaled background model, we performed the same design experiment with identical inversion parameters and noise characteristics.

[Figure 10 about here.]

Figure 10 shows the results of the high-contrast experiment including the test perturbation in panel [A] (same as previous test), the inversion result for the initial geometry guess in panel [B], and the differential tomogram generated by the optimal geometry in panel [C]. The Multilevel Coordinate Search process converged in a similar number of iterations with a similar l_2 misfit reduction (0.0013345 to 0.0008937). The design results are quite different; the "initial" inversion result is of lower quality than in first test because of decreased ray coverage in the low velocity zone. Because first arrivals are dominated by headwaves around the boundary of the plume, the resolution of the plume interior is less focused. The optimized geometry is also significantly different than the prior example; the array is shifted up and constrained in aperture but it does not exhibit the pronounced asymmetry of the earlier design. The improved design clearly enhances image quality in comparison to the naive design but cannot recover the "kink" in the plume as accurately as in the low contrast case. This example demonstrates the strong dependence of optimal designs on the choice of background model, which is not surprising since $\mathbf{m}_{base}$ controls ray coverage and the structure of $\mathbf{G}$ for any given choice of geometry.

Although slightly more realistic, these two simple examples have several clear limitations; mainly that only a single time-step of the flow process was incorporated as a test perturbation in Ω_u and that only the linearized design problem is considered despite the fact that the magnitude of the

perturbation is probably outside the linear regime. Ideally, Ω_u would include the entire time history of the flow process in the design problem so as to allow imaging of each temporal stage of plume evolution. If computational resources allowed, multiple flow realizations could be used to encompass inevitable uncertainty in subsurface permeability structure. Our use of a linearized imaging test is a second significant limitation; with large velocity perturbations, secondary ray bending due is inevitable and might significantly alter the optimal design, as could be inferred by our scaling test of $\mathbf{m}_{base}$. As mentioned previously, the same formulation for Ω_u could be used to tackle the non-linear case but the differential tomography approach (i.e. inverting time differences) would have to be discarded since $\mathbf{\Delta d}$ would involve a subtraction of times sampling different regions of space.

The Next-Generation Permanent Monitoring Array?

While the crosswell arrays shown in the first three examples were small (8 x 80 and 6 x 48), future pilot deployments are likely to be even sparser due to cost constraints. The number of source levels in particular will likely dominate project budgets. With this reality in mind, we solved the two parameter optimal design problem for source arrays with 2, 4, and 6 levels and a 48 level receiver array using checkerboard test patterns. Figure 11 shows the test model (panel [A]) besides the optimal geometries for this set of source array sizes. All three geometries provide some degree of resolution near the receiver well; however, increasing the number of sources provides the coverage and aperture needed to effectively image features near the source well and in the central portion of the imaging target. All three designs also exhibited the asymmetric array lengths present in previous optimal design experiments. Surprisingly, a minimal array with only 6 sources was able to effectively image features across the entire target unit suggesting that similar arrays could provide useful real-time tomographic imagery when permanently installed in the well-bore.

[Figure 11 about here.]

CONCLUSIONS

Through the examples shown in this paper, we have demonstrated the benefit of optimal design algorithms when applied to the refinement of crosswell seismic acquisition geometries. Our approach combines a simple l_2 image-based experiment quality metric, a parsimonious representation of survey geometry, and a robust direct search method. These optimal design components were applied to differential seismic traveltime tomography, a developing imaging technique with application to *in situ* monitoring of flow processes. The resulting methodology performs well for both two and four parameter optimal experiment design problems and scales to models for which evaluation of SVD metrics would be prohibitively expensive. Our investigation of optimal crosswell monitoring arrays for geometries with significantly fewer sources than receivers has yielded the following observations,

1. Tomographic image quality can be improved by incorporating asymmetry into the length of source and receiver arrays.

2. In addition to asymmetric cable lengths, the resolution of dipping features can potentially benefit from a vertical offset between the two arrays.

3. Useful tomographic imagery can be derived from sparse asymmetric crosswell data, thus opening the door to continuous monitoring of flow processes from within the reservoir.

The examples shown in this paper have been limited to ray-theoretic traveltime tomography. The added benefit of using later arrivals, particularly reflections, in crosswell imaging has been well-established. An important step in exploration of design algorithms will be to incorporate wavefield

imaging methods into the same design framework. Arrays tailored to wavefield imaging will likely have different characteristics than those designed purely for traveltime tomography due to their different spatial sensitivity patterns. Traditional wavefield processing also requires attention to spatial aliasing, such constraints could easily be added to the formulation as soft penalty terms. Equally important challenges remain in adapting the design strategy to truly non-linear imaging formalisms which do not require recourse to assumptions concerning small velocity perturbations.

Our examination of two deterministic search algorithms suggests that Nelder-Mead is useful in low-dimensional design problems where the objective function is close to unimodal. For more complicated problems, a global optimization algorithm is almost certainly required but the Nelder-Mead algorithm may have some utility after a "hot start" places it near the global minimum. For the 4 dimensional design problem, Multilevel Coordinate Search reliably converged to high quality designs provided only with weak bounds on the design variables. Not having compared the Multilevel Coordinate Search algorithm to other global optimization techniques, we cannot come to any conclusions concerning its superiority to more commonly used approaches based on simulated annealing or genetic algorithms.

While we are strong advocates of parsimonious descriptions of experiment geometry, exactly how many parameters should be used is a topic open for discussion. Additional degrees of freedom could include linear, quadratic, or higher order variations in source/receiver spacing. While providing this extra flexibility would likely provide some improvement to image quality, the costs of custom fabrication might outweigh these benefits. Ideally, all budgetary components of the survey would be rolled into a single objective function which would provide a trade-off curve between total acquisition cost and image quality. An even more ambitious approach would pose the experiment

quality metric in a probabilistic hypothesis testing framework, thus allowing us to formally quantify the cost of accurately answering questions about the subsurface. Our route, while considerably less ambitious, provides useful design parameters which can be calculated in finite time with available computational resources.

ACKNOWLEDGMENTS

The first author would like to thank the Founding Members Consortium of the Earth Resources Laboratory for support during the early stages of this research. Secondary support was provided by the GEOSEQ project, National Energy Technology Laboratory, U.S. Department of Energy, under contract no. DE-AC02-05CH11231. The author benefited from a broad range of discussions with Prof. M. Nafi Toksoz, Prof. Jerry Harris, Darrel Coles, Burke Minsley, Susan Hubbard, and Tom Daley. Chris Doughty (Lawrence Berkeley National Laboratory) provided the TOUGH2 multiphase flow modeling results used in example 3. We would also like to thank Prof. Colin Zelt for making the source code for the FAST eikonal solver publicly available.

REFERENCES

Ajo-Franklin, J., C. Doughty, and T. Daley, 2007a, Integration of continuous active-source seismic monitoring and flow modeling for CO_2 sequestration: The Frio II brine pilot, *in* EOS Trans. AGU Fall Meet. Suppl., volume **88**, American Geophysical Union.

Ajo-Franklin, J., B. Minsley, and T. Daley, 2007b, Applying compactness constraints to differential traveltime tomography: Geophysics, **72**, R67–R75.

Aldridge, D. and D. Oldenburg, 1993, Two-dimensional tomographic inversion with finite-difference traveltimes: Journal of Seismic Exploration, **2**, 257–274.

Barth, N. and C. Wunsch, 1990, Oceanographic experiment design by simulated annealing: J. Phys. Ocean., **20**, 1249–1263.

Batzle, M. and Z. Wang, 1992, Seismic properties of pore fluids: Geophysics, **57**, 1396–1408.

Blanco, J., S. Knudsen, and F. Bostick, 2006, Time-lapse VSP field test for gas reservoir monitoring using permanent fiber optic seismic system: 76th Annual International Meeting, Expanded Abstracts, 3447–3451, Soc. of Expl. Geophysics.

Box, G. and H. Lucas, 1959, Design of experiments in non-linear situations: Biometrika, **47**, 77–90.

Curtis, A., 1999a, Optimal design of focused experiments and surveys: Geophysical Journal International, **139**, 205–215.

———, 1999b, Optimal experiment design : cross-borehole tomographic examples: Geophysical Journal International, **136**, 637–650.

Curtis, A., A. Michelini, D. Leslie, and A. Lomax, 2004, A deterministic algorithm for experimental design applied to tomographic and microseismic monitoring surveys: Geophysical Journal International, **157**, 595–606.

Curtis, A. and R. Snieder, 1997, Reconditioning inverse problems using the genetic algorithm and

revised parametrization: Geophysics, **62**, 524–1532.

Daley, T., L. Myer, and E. Majer, 2005, Acquisition of time-lapse, 6-component, P- and S-wave, crosswell seismic survey with an orbital vibrator and of time-lapse VSP for CO_2 injection monitoring: Presented at the 75th Ann. Internat. Mtg, Soc.Of Expl. Geophysocs.

Daley, T., L. Myer, J. Peterson, E. Majer, and . G. Hoversten, 2007a, Time-lapse crosswell seismic and vsp monitoring of injected CO_2 in a brine aquifer: Environmental Geology.

Daley, T. M., J. B. Ajo-Franklin, and . C. Doughty, 2008, Integration of crosswell CASSM (Continuous Active Source Seismic Monitoring) and flow modeling for imaging a CO_2 plume in a brine aquifer: Presented at the 78th Annual International Meeting, Expanded Abstracts, Soc.Of Expl. Geophysics.

Daley, T. M., R. D. Solbau, . J. B. Ajo-Franklin, and S. M. Benson, 2007b, Continuous active-source seismic monitoring of CO_2 injection in a brine aquifer: Geophysics, **72**, A57–A61.

Dixon, L. and G. Szego, 1978, The global optimization problem an introduction, *in* Dixon, L. and G. Szego, eds., Towards Global Optimization 2, 1–15, North-Holland.

Dutta, N. and H. Ode, 1979, Attenuation and dispersion of compressional waves in fluid-filled porous rocks with partial gas saturation (White model) - Part 1: Biot theory, Part 2 : Results: Geophysics, **44**, 1777–1805.

Galbraith, M., 2004, A new methodology for 3d survey design: The Leading Edge, 1017–1023.

Hole, J. and B. Zelt, 1995, 3-D finite-difference reflection traveltimes: Geophysical Journal International, **121**, 427–434.

Hovorka, S., S. Benson, C. Doughty, B. Freifeld, . S. Sakurai, T. Daley, Y. Kharaka, M. Holtz, R. T. S. Nance, and L. M. andK.G. Knauss, 2006, Measuring permanence of CO_2 storage in saline formations : the Frio experiment: Environmental Geosciences, **13**, 1–17.

Huyer, W. and A. Neumaier, 1999, Global optimization by multilevel coordinate search: Journal of Global Optimization, **14**, 331–355.

John, R. and N. Draper, 1975, D-optimality for regression designs a review: Technometrics, **17**, 15–23.

Jones, D., C. Perttunen, and B. Stuckman, 1993, Lipschitizian optimization without the lipschitz constant: Journal of Optimization Theory and Applications, **79**, 157–181.

Lazaratos, S. and B. Marion, 1997, Crosswell seismic imaging of reservoir changes caused by CO_2 injection: The Leading Edge, **16**, 1300–1306.

Lemmon, E., M. McLlinden, and D. Friend, 2005, Thermophysical properties of fluid systens, *in* Linstrom, P. and W. Mallard, eds., NIST Chemistry WebBook, NIST Standard Reference Database Number 69, National Institute of Standards and Technology.

Leveque, J.-J., L. Rivera, and G. Wittlinger, 1993, On the use of the checker-board test to assess the resolution of of tomographic inversions: Geophysical Journal International, **115**, 313318.

Liner, C., W. Underwoord, and R. Gobeli, 1999, 3-d seismic survey design as an optimization problem: The Leading Edge, 1054–1060.

Maurer, H. and D. Boerner, 1998, Optimized and robust experimental design : a non-linear application to EM sounding: Geophysical Journal International, **132**, 458–468.

Menke, W., 1984, Geophysical data analysis : Discrete inverse theory: Academic Press.

Morrice, D., A. Kenyon, and C. Beckett, 2001, Optimizing operations in 3-d land seismic surveys: Geophysics, **66**, 1818–1826.

Muzic, R., A. Nelson, G. Saidel, and F. Miraldi, 1996, Optimal experiment design for pet quantification of receptor concentration: IEEE Transactions on Medical Imaging, **15**.

Nelder, J. and R. Mead, 1965, A simplex method for function minimization: The Computer Journal,

7, 308–313.

Paige, C. and M. Saunders, 1982, An algorithm for sparse linear equations and sparse least squares: ACM Transactions in Mathematical Software, **8**, 43–71.

Press, W., B. Flannery, S. Teukolsky, and . W. Vetterling, 1992, Numerical recipes in c : The art of scientific computing: Cambridge University Press.

Pruess, K. and N. Spycher, 2007, Eco2n a fluid property module for the tough2 code for studies of co2 storage in saline aquifers: Energy Conversion and Management, **48**, 1761–1767.

Ross, C. and S. Altan, 1997, Time-lapse seismic monitoring: Some shortcomings in nonuniform processing: The Leading Edge, **16**, 931–937.

Routh, P., G. Oldenborger, and D. Oldenburg, 2005, Optimal survey design using the point spread function measure of resolution: Presented at the Proceedings Of The 75th Ann. Mtg.

Sethian, J. and A. M. Popovici, 1999, 3-D traveltime computation using the fast marching method: Geophysics, **64**, 516–523.

Smit, F., M. Ligtendag, P. Wills, and R. Calvert, 2006, Towards affordable permanent seismic reservoir monitoring using the sparse OBC concept: The Leading Edge, 454–459.

Stummer, P., H. Maurer, H. H. and A. G. Green, 2002, Optimization of dc resistivity data acquisition : real-time experimental design and a new multielectrode system: IEEE Transactions on Geoscience and Remote Sensing, **40**, 2727–2735.

Thompson, M., L. Amundsen, P. Karstadand, J. Langhammer, . H. Nakstad, and M. Eriksrud, 2006, Field trial of fibre-optic multi-component sensor system for application in ocean bottom seismic: Proceedings Of The 93rd Ann. Mtg, Expanded Abstracts, 1148–1152, Soc. of Expl. Geophysics.

van den Berg, J., A. Curtis, and J. Trampert, 2003, Optimal nonlinear Bayesian experimental design

: an application to amplitude versus offset experiments: Geophysical Journal International, **155**, 411–421.

Vermeer, G., 2003, 3d seismic survey optimization: The Leading Edge, 934–941.

Vesnaver, A., F. Accaino, G. Bohm, G. Madrussani, . J. Pajchel, G. Rossi, and G. D. Moro", 2003, Time-lapse tomography: Geophysics, **68**, 815–823.

Vidale, J., 1988, Finite-difference calculation of travel times: Bull. Seis. Soc. Of America, **78**, 2062–2076.

Walter, E. and L. Pronzato, 1987, Optimal experiment design for nonlinear models subject to large prior uncertainties: American Journal of Physiology, **253**, 530–534.

White, J., 1975, Computed seismic speeds and attenuation in rocks with partial gas saturation: Geophysics, **40**, 224–232.

List Of Figures

1. A test checkerboard with various target screens : The left panel [A] shows a global checkerboard with square 2 m cells while the middle and right panels depict targeted windows of this test model confined to either a horizontal [B] or dipping [C] layers.

2. Design variables for a two parameter crosswell geometry : The search problem is posed in terms of choosing optimal source (P_1) and receiver (P_2) array dimensions. The target is a depth limited checker-board intended to replicate the reservoir unit targeted for monitoring.

3. Experiment quality metric for the 2 parameter problem evaluated on a regular grid : Note the trough-shaped minimum corresponding to a narrow range of source array 1/2 widths near 6 m.

4. The l_2 objective function surface and 3 designs for the (P_1, P_2) search problem : The top panel depicts the combined objective function sampled on a regular mesh with 3 particular solutions labeled. The bottom panels show the true perturbation model (A), and reconstructed images corresponding to a minimal array (B), a "optimal" array (C), and a wide aperture array (D).

5. A comparison of the convergence of the Nelder-Mead downhill simplex (NM, shown in the top panel) and the global Multilevel Coordinate Search (MCS, shown in the bottom panel) algorithms. The bold squares indicate the global optimum which both methods converge to. The bold red circle on the left panel indicates the Nelder-Mead starting model.

6. Design variables for a four parameter crosswell geometry : The search problem is posed in terms of choosing optimal source and receiver array depths (P_1, P_2) and 1/2 widths (P_3, P_4). The target is a depth limited checker-board intended to replicate the reservoir unit targeted

for monitoring, in this case possibly tilted to replicate geologic dip.

7. Optimal crosswell design for a four parameter system : Shown are the true model perturbation [A], followed by the inversion results for an initial guess at $\mathbf{q}$ [B], and the final optimized experiment [C].

8. Base Velocity Model and Estimate of Flow-Induced Velocity Perturbations at Frio : Panel [A] depicts a log-derived background model used for the the experiment design test while panel [B] shows an estimate of the CO_2 induced velocity perturbation derived from multi-phase flow modeling results. The dipping black lines in panel [B] are background model isocontours.

9. Optimal crosswell design for a four parameter system with a flow-based test pattern: Shown are the true model perturbation [A], followed by the inversion results for an initial guess at $\mathbf{q}$ [B], and the final optimized experiment [C].

10. Optimal crosswell design for a flow-based test pattern with a high velocity contrast background ($\mathbf{m}_{base}$): Shown are the true model perturbation [A], followed by the inversion results for an initial guess at $\mathbf{q}$ [B], and the final optimized experiment [C].

11. Optimal Designs for three sparse arrays : Panel [A] depicts the true checkerboard model while panels [B],[C], and [D] show the optimal acquisition geometries for 2, 4, and 6 sources respectively.

LIST OF FIGURES

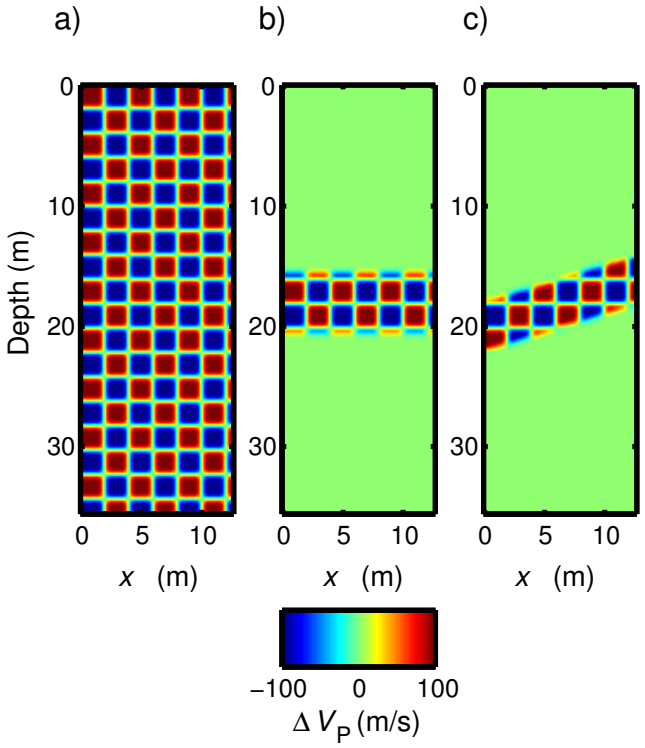

Figure 1: A test checkerboard with various target screens : The left panel [A] shows a global checkerboard with square 2 m cells while the middle and right panels depict targeted windows of this test model confined to either a horizontal [B] or dipping [C] layers.

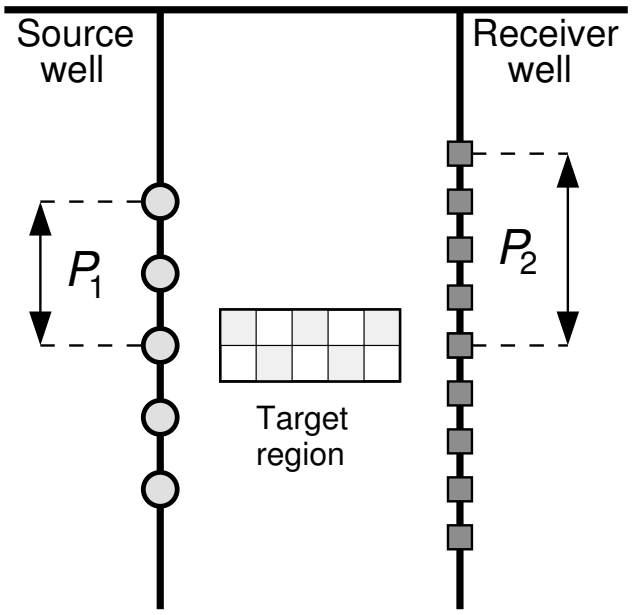

Figure 2: Design variables for a two parameter crosswell geometry : The search problem is posed in terms of choosing optimal source (P_1) and receiver (P_2) array dimensions. The target is a depth limited checker-board intended to replicate the reservoir unit targeted for monitoring.

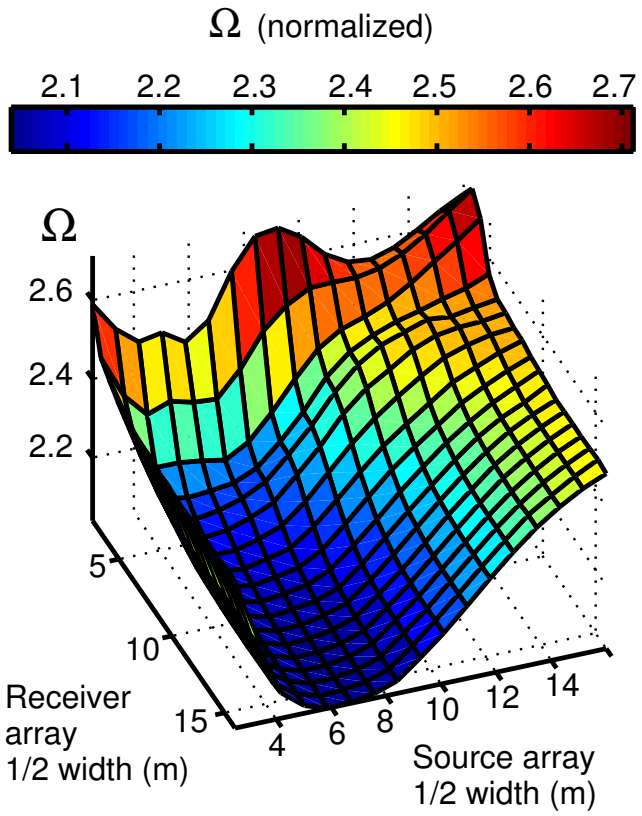

Figure 3: Experiment quality metric for the 2 parameter problem evaluated on a regular grid : Note the trough-shaped minimum corresponding to a narrow range of source array 1/2 widths near 6 m.

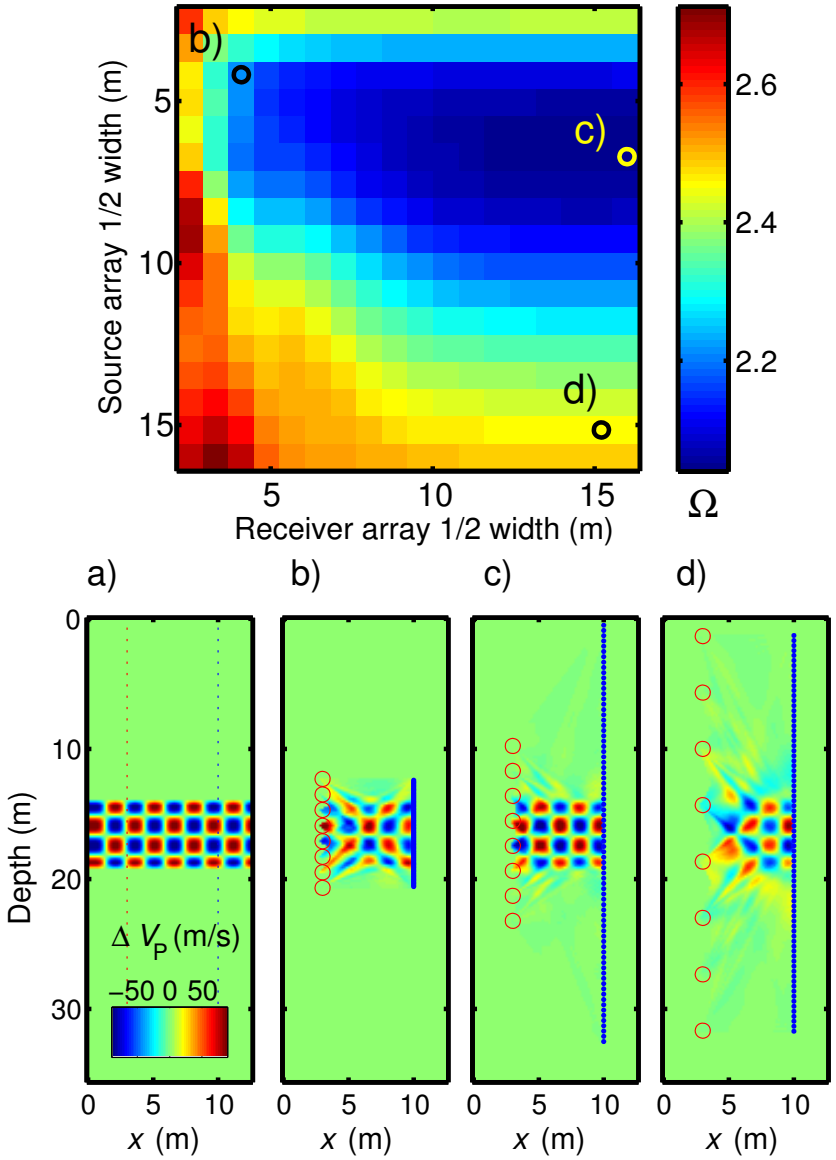

Figure 4: The l_2 objective function surface and 3 designs for the (P_1, P_2) search problem : The top panel depicts the combined objective function sampled on a regular mesh with 3 particular solutions labeled. The bottom panels show the true perturbation model (A), and reconstructed images corresponding to a minimal array (B), a "optimal" array (C), and a wide aperture array (D).

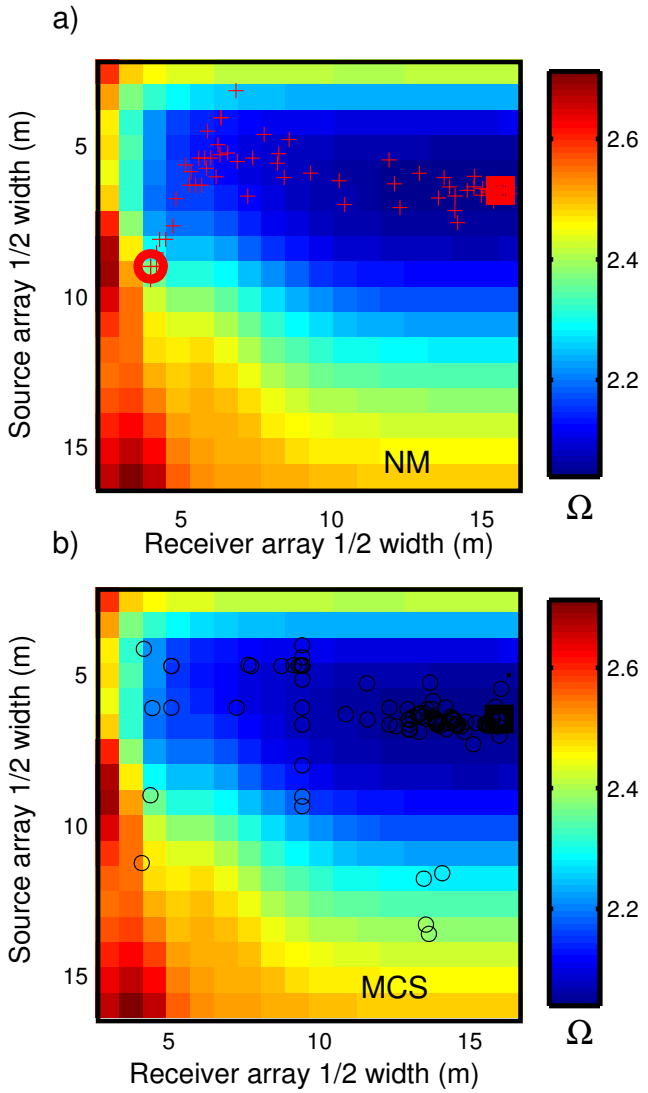

Figure 5: A comparison of the convergence of the Nelder-Mead downhill simplex (NM, shown in the top panel) and the global Multilevel Coordinate Search (MCS, shown in the bottom panel) algorithms. The bold squares indicate the global optimum which both methods converge to. The bold red circle on the left panel indicates the Nelder-Mead starting model.

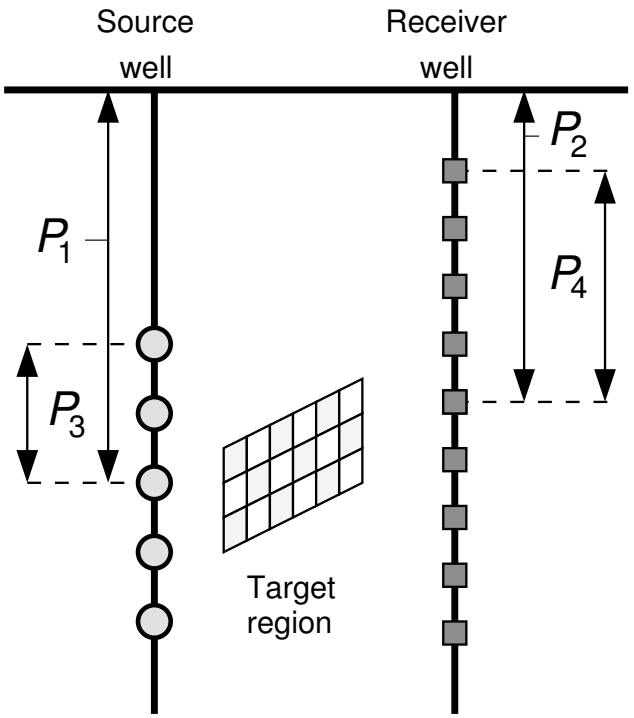

Figure 6: Design variables for a four parameter crosswell geometry : The search problem is posed in terms of choosing optimal source and receiver array depths (P_1, P_2) and 1/2 widths (P_3, P_4). The target is a depth limited checker-board intended to replicate the reservoir unit targeted for monitoring, in this case possibly tilted to replicate geologic dip.

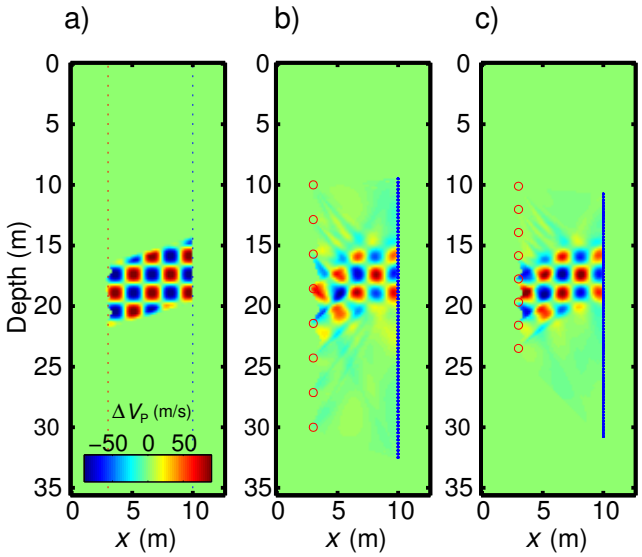

Figure 7: Optimal crosswell design for a four parameter system : Shown are the true model perturbation [A], followed by the inversion results for an initial guess at $\mathbf{q}$ [B], and the final optimized experiment [C].

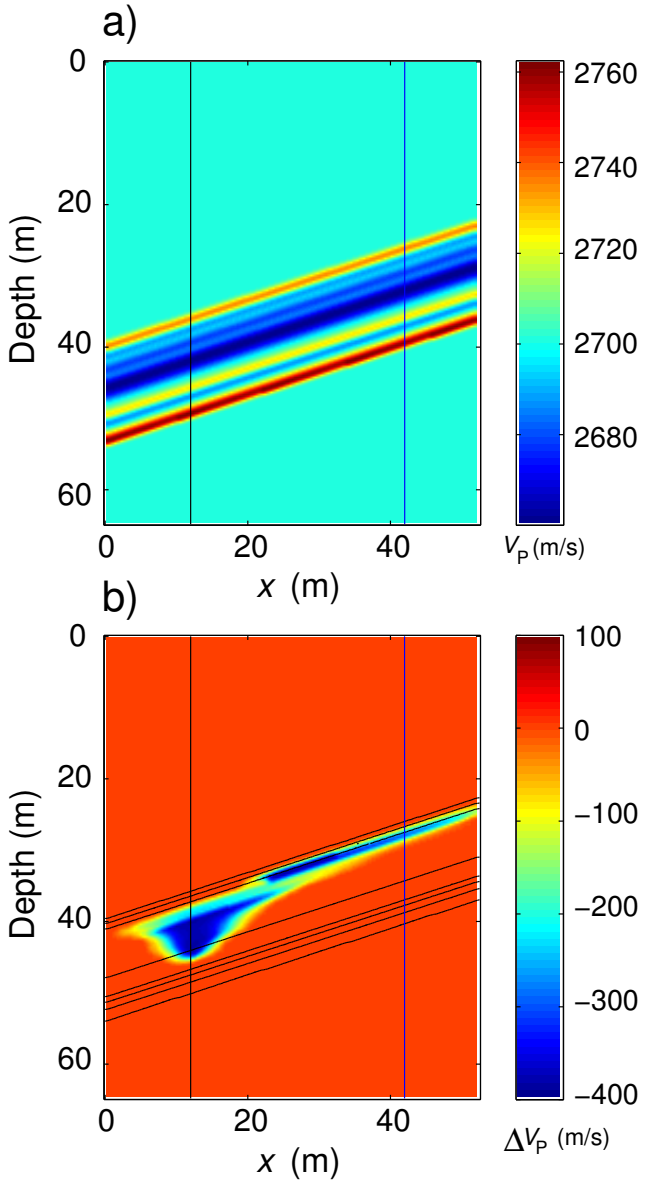

Figure 8: Base Velocity Model and Estimate of Flow-Induced Velocity Perturbations at Frio : Panel [A] depicts a log-derived background model used for the the experiment design test while panel [B] shows an estimate of the CO_2 induced velocity perturbation derived from multi-phase flow modeling results. The dipping black lines in panel [B] are background model isocontours.

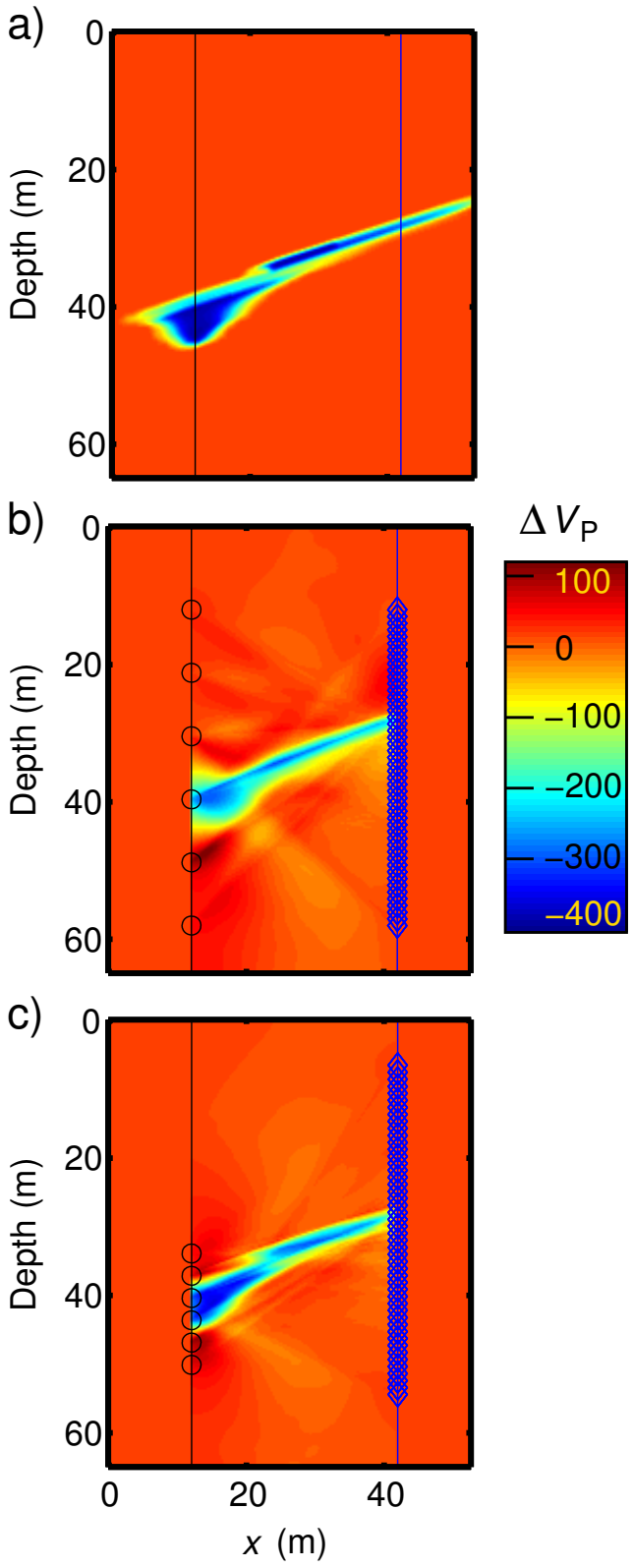

Figure 9: Optimal crosswell design for a four parameter system with a flow-based test pattern: Shown are the true model perturbation [A], followed by the inversion results for an initial guess at $\mathbf{q}$ [B], and the final optimized experiment [C].

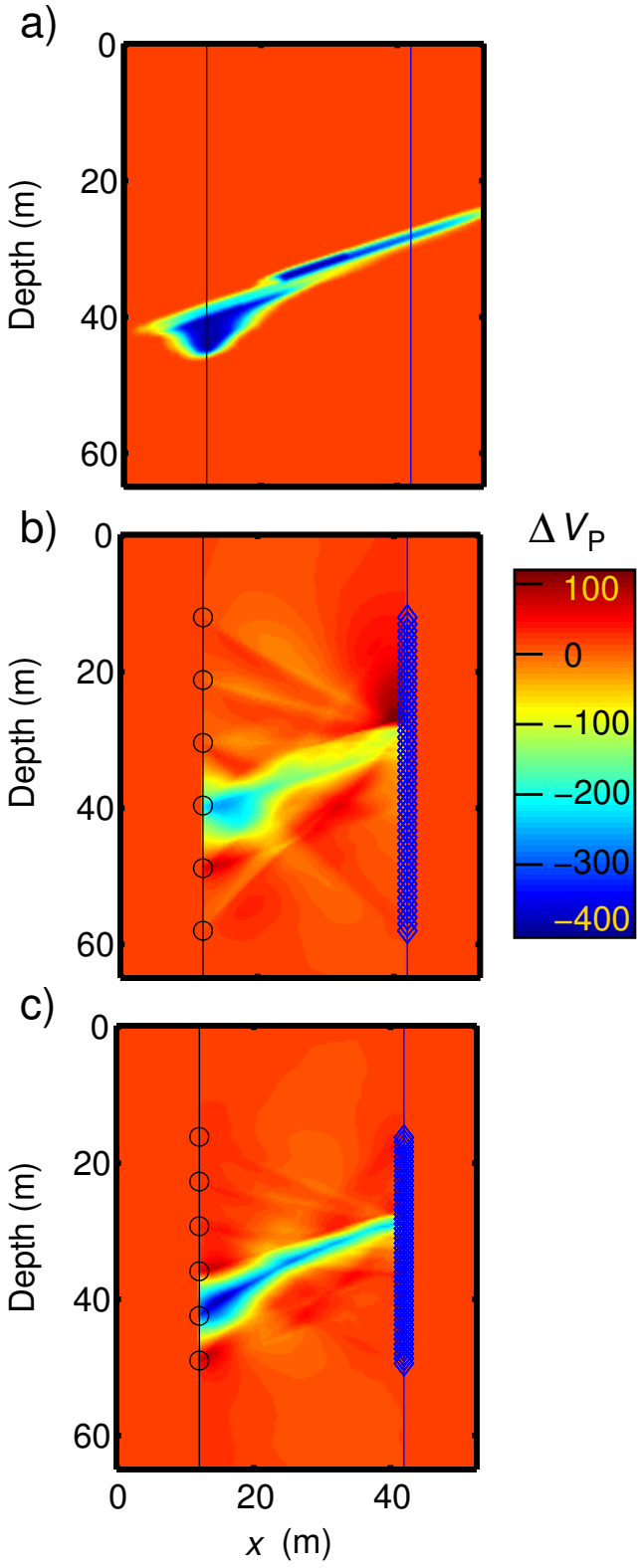

Figure 10: Optimal crosswell design for a flow-based test pattern with a high velocity contrast background ($\mathbf{m}_{base}$): Shown are the true model perturbation [A], followed by the inversion results for an initial guess at $\mathbf{q}$ [B], and the final optimized experiment [C].

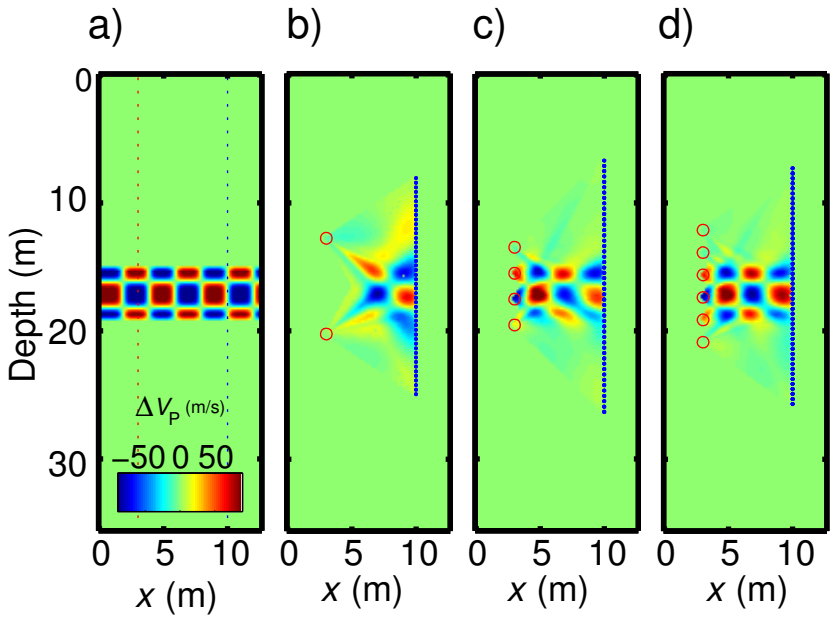

Figure 11: Optimal Designs for three sparse arrays : Panel [A] depicts the true checkerboard model while panels [B],[C], and [D] show the optimal acquisition geometries for 2, 4, and 6 sources respectively.